Journal of Oceanology and Limnology
Vol. 44, No. 5, pp. 1813-1832, 2026
https://doi.org/10.1007/s00343-026-5533-6

Research Paper

Global sensitivity analysis of critical factors in radiometric benchmark transfer over oceanic pseudo-invariant sites*

Shanqi WANG[1], Qingjun SONG[2], Ling SUN[3, 4], Liqiong CHEN[1], Xi CHEN[1], Liqiao TIAN[1, **]

[1] *State Key Laboratory of Information Engineering in Surveying, Mapping and Remote Sensing, Wuhan University, Wuhan 430079, China*

[2] *National Satellite Ocean Application Service, Ministry of Natural Resources of the People's Republic of China, Beijing 100081, China*

[3] *Key Laboratory of Radiometric Calibration and Validation for Environmental Satellites, China Meteorological Administration/ National Satellite Meteorological Center (National Center for Space Weather), Beijing 100081, China*

[4] *Xu Jianmin Meteorological Satellite Innovation Center, Beijing 100081, China*

Received Dec. 25, 2025; accepted in principle Mar. 30, 2026; accepted for publication Jun. 15, 2026

© Chinese Society for Oceanology and Limnology, Science Press and Springer-Verlag GmbH Germany, part of Springer Nature 2026

Abstract A global sensitivity analysis of critical factors in radiometric benchmark transfer is conducted in this study using oceanic pseudo-invariant sites to quantify and control transfer uncertainty under non-ideal matching conditions. Prior to the sensitivity analysis, oceanic pseudo-invariant sites are objectively identified through a screening procedure to ensure long-term radiometric stability under varying environmental conditions. Single-parameter sensitivity pre-screening is first performed to identify environmental variables that significantly affect the transfer quality at the optimally selected pseudo-invariant sites. The resulting multidimensional parameter space is defined by the following parameters: viewing zenith angle, solar zenith angle, relative azimuth angle, aerosol optical thickness at 550 nm, wind speed, and discrete spectral wavelength. A variance-based Sobol global sensitivity analysis driven by low-discrepancy sequence sampling was then conducted at 40 discrete wavelengths spanning 412–945 nm. Results indicate that, across all bands, differences in top-of-atmosphere (TOA) reflectance are dominated by angular-domain parameters. At 443 nm, for example, the sum of first-order sensitivity indices exceeds 0.99, while the normalized contributions from non-angular uncertainty sources are below 0.01; total-effect indices closely match the first-order indices, indicating weak higher-order interactions. Under these conditions, contributions from different uncertainty domains can be combined through the addition of the standard uncertainties within each domain. The proposed framework enables a transition from traditional cross-matching, focusing on spatio-temporal matching, toward sensitivity-guided geometric matching constraints and correction strategies, providing quantitative support for uncertainty budgeting and subsequent correction scheme design in ocean-satellite radiometric benchmark transfer and cross-calibration.

Keyword: radiometric benchmark transfer; global sensitivity analysis; uncertainty quantification; oceanic pseudo-invariant site

1 INTRODUCTION

Currently, satellite radiometric calibration is evolving from ensuring self-consistency within a single payload to cross-platform radiometric harmonization enabled by ultra-stable, ultra-high-accuracy reference (benchmark) instruments (Lu et al., 2020). A radiometric benchmark satellite transfers national laboratory radiance standards and quantity-dissemination techniques into space, enabling on-orbit SI-traceable calibration of its benchmark

* Supported by the National Key Research and Development Program of China (Nos. 2023YFB3905300, 2023YFB3905304)

** Corresponding author: tianliqiao@whu.edu.cn

instrument and delivering the highest level of radiometric accuracy. By conducting co-located observations with identical acquisition time and observation geometry between the benchmark and target satellites, inter-satellite radiometric value transfer can be achieved, ensuring a consistent radiometric reference across missions and enabling joint use and comparison of long-term multi-satellite data records (Dai et al., 2025). To support this transition, some high-precision benchmark missions are being prepared for launch, including ESA's Traceable Radiometry Underpinning Terrestrial- and Helio-Studies (TRUTHS) and NASA's Climate Absolute Radiance and Refractivity Observatory (CLARREO) Pathfinder (CPF). These missions will serve as metrology laboratories in space by providing a measurement-standard (SI-traceable) on-orbit inter-calibration reference for other lower-resolution Earth observation instruments (Gorroño et al., 2017, 2024; Goldin et al., 2019; Fox and Green, 2020). China has also proposed the concept of space radiation measurement reference technology and is likely to launch a radiometric benchmark satellite in the near future, aiming to achieve direct SI traceability for satellite-based radiometric observations (Lu et al., 2020).

In the link of radiometric benchmark transfer, mismatches between the benchmark (reference) satellite and the target satellite observations typically span four interconnected domains: temporal, spatial, spectral, and angular. These mismatches arise from several factors: non-simultaneous acquisitions that allow atmospheric and sea-state conditions to change; differences in ground-sampling distance and registration accuracy; disparities between the spectral-response functions of the two instruments; and deviations in solar-sensor viewing geometry that introduce BRDF-related errors (Hu et al., 2024). Under such "non-ideal", "loose" matching observation conditions, a vector Radiative Transfer Model (RTM) for the coupled ocean-atmosphere system can be used to simulate and analyze top-of-atmosphere simulations over radiometrically stable targets, thereby enabling radiometric benchmark transfer from the reference to the target satellite with flexible matching constraints and controllable uncertainty; the subsequent RTM-based correction can compensate for radiance differences induced by these non-idealities, yielding results comparable to ideal observation conditions (Sun et al., 2012). Building on this foundation, conducting the radiometric transfer over open-ocean gyre regions can minimize the temporal variability of the water-leaving radiance signal (Chen et al., 2020). Subsequently, through reasonable matching conditions constraints, the approach combining the strengths of Simultaneous Nadir Overpass (SNO) and Pseudo-Invariant Calibration Site (PICS) methodologies offers dual advantages: it exploits the radiometric stability of the selected target site and mitigates the errors introduced by RTM-based corrections, thereby reducing the overall uncertainty of the radiometric transfer (Hu et al., 2024).

The radiometric benchmark transfer target area considered in this study—the ocean—represents a quintessential low-energy radiance scene in the reflective solar bands (RSBs). Here, the water-leaving radiance accounts for only about 10% of the total top-of-atmosphere nadir radiance (Holmes et al., 2018; Qiao et al., 2025). At the same time, ocean gyre regions far from land exhibit high spatial homogeneity and temporal stability, making them ideal radiometric benchmark transfer media for low-energy radiance in the reflective spectrum. When dealing with the weak signal of marine water, existing studies face challenges such as limited radiometric dynamic range and stringent requirements for detecting water color constituents. Ocean color sensors are specifically designed with high radiometric sensitivity to capture these extremely weak marine signals. Consequently, viewing traditional bright terrestrial calibration sites (e.g., the Libyan Desert) essentially "blinds" these sensors, causing severe radiometric saturation (Teillet et al., 2007; Angal et al., 2016). Furthermore, the spectral shape of desert targets—heavily peaking in the red and near-infrared—drastically diverges from that of oligotrophic oceans, which peak in the blue and decay exponentially toward the near-infrared (Gordon, 1997; Mishra et al., 2014; Zibordi et al., 2025). Additionally, the measurement signal of an ocean color sensor that is highly sensitive to observation geometry conditions (Gordon and Wang, 1994); moreover, pixels with smaller solar zenith angles are more susceptible to sun-glint contamination (Cox and Munk, 1954).

With the rapid development of medium- and high-resolution ocean satellite technology, increasingly stringent requirements are being placed on the accuracy and stability of radiometric benchmark transfer. High-resolution observations can reveal finer-scale details of air-sea interface coupling but they simultaneously introduce a more complex radiometric transfer regime. Wind-driven variations in sea surface roughness alter reflectance characteristics; as wind

speed increases, the coverage of whitecaps generated by wave breaking expands. These transient and non-stationary features over the open ocean markedly amplify the signal received by satellite sensors, thereby magnifying the associated radiometric transfer uncertainties (Stramska and Petelski, 2003). These emerging challenges require us to further deepen the understanding of the radiation characteristics of oceanic pseudo-invariant sites and develop more accurate and efficient full-link analysis and uncertainty assessment methods for the radiometric benchmark transfer.

The radiative transfer link involves multiple complex contributing factors associated with coupled water-interface-atmosphere radiative processes. For example, the type, concentration, and spatial distribution of aerosols in the atmosphere have an important influence on the optical thickness of the atmosphere by changing the scattering and absorption characteristics in the radiative transfer path. This has a complex effect on the observation of reflected radiation on the ocean surface (Li et al., 2017b; Song et al., 2023; Hannadige et al., 2023). Moreover, the radiation characteristics of oceanic targets are strongly modulated by observation geometry, including the solar zenith angle (SZA), the satellite view zenith angle (VZA), and the relative azimuth angle (RAA). These geometric parameters affect both the angle at which solar energy reaches the sea surface and the path along which the reflected signal returns to the sensor. When the solar zenith angle is small, specular reflection dominates, producing a sharp reflectance peak known as sun glint; at larger solar zenith angle, the share of diffuse reflection increases; the combined influence of a high solar zenith angle and stronger winds broadens the glint pattern, leading to a spatially "smeared" or dispersed glint zone (Gatebe et al., 2005). Therefore, it is of great significance to study the full-link process of radiometric benchmark transfer. This process encompasses multiple interacting links, such as sea-air interface coupling and atmospheric radiation transmission. The noise introduced by each link will affect the final radiation signal, thus affecting the accuracy and reliability of the benchmark transfer. Detailed analysis of these links can identify and quantify various sources of uncertainty and support reducing transmission uncertainties through appropriate correction models.

In summary, this study focuses on the current radiometric benchmark transfer link from reference instruments to target instruments via oceanic pseudo-invariant sites, a link that has not yet been systematically and quantitatively analyzed. At present, cross-calibration using target fields is usually based on land targets such as the Libyan desert, rather than on low-energy radiance ocean targets (Gorroño et al., 2017; Hu et al., 2024; Ma et al., 2025). Meanwhile, previous studies on the marine radiometric transfer chain have predominantly employed the Simultaneous Nadir Observation (SNO) method (Chen et al., 2020), lacking a unified approach that can quantify uncertainty sources across the entire parameter space and elucidate their interaction mechanisms. Therefore, based on the high temporal and spatial stability of the oceanic pseudo-invariant site, this study employs the Ordres Successifs Ocean Atmosphere Avance (OSOAA) model to simulate top-of-atmosphere radiative signals, combined with the Sobol global sensitivity analysis framework of low-discrepancy sequence sampling. With this framework, this study systematically evaluates the contribution of the radiation difference of the benchmark transfer in time, space, spectrum, and angle domains to the atmospheric top reflectivity and its coupling mechanism in the process of radiometric benchmark transfer from the reference satellite to the medium and low-resolution target (marine) satellite. This approach provides a quantifiable, closed-loop uncertainty control path for the radiometric benchmark transfer, offering a quantitative basis for correcting radiometric differences during the benchmark transfer process.

2 DATA SCREENING: OPTIMAL SELECTION OF OCEANIC PSEUDO-INVARIANT SITES

Internationally recommended oceanic pseudo-invariant sites include the North Pacific Gyre (NPG), South Pacific Gyre (SPG), North Atlantic Gyre (NAG), South Atlantic Gyre (SAG), and South Indian Gyre (SIG), with their specific locations listed in Table 1 (Fougnie et al., 2002; Morel et al.,

Table 1 Locations of internationally recommended oceanic pseudo-invariant sites

Site	Longitude range	Latitude range
NAG	70°W–45°W	22°N–27°N
NPG	150°E–165°E	10°N–20°N
SIG	70°E–90°E	30°S–21°S
SPG	125°W–100°W	30°S–20°S
SAG	32°W–25°W	22.5°S–12.5°S

2010; Chen et al., 2022). These pseudo-invariant sites are located in open circulation sea areas far away from continental pollution sources: In terms of atmospheric radiation characteristics over the sites, atmospheric interference from aerosols is lower and more stable over long time series, which is beneficial to minimize the temporal domain changes of the water-leaving signals during the radiometric benchmark transfer and thereby reduce temporal domain uncertainty (Chen et al., 2020), the aerosol type is mainly marine aerosol, and the aerosol optical thickness remains low in the visible spectral band (Smirnov et al., 2002; Saliba et al., 2020; Sakerin et al., 2022; Dournaux et al., 2025). With respect to water radiation characteristics, the water bodies in these sites are characterized by typical oligotrophic conditions, and their chlorophyll concentrations usually remain exceedingly low (Morel et al., 2010). The enduring, ultra-low-chlorophyll nature of these waters imparts a high degree of spatiotemporal homogeneity to the water-leaving signals observed over them. Selecting such an oceanic pseudo-invariant site for radiometric benchmark transfer therefore enables the benchmark to be propagated with both universality and long-term consistency across a wide range of climatic and geographic conditions.

In this study, the optimal selection of the oceanic pseudo-invariant site involves establishing a spatial grid with 1°×1° intervals for each of the five recommended oceanic pseudo-invariant sites listed in Table 1. Based on MODIS data products and ERA5 reanalysis data from January 1, 2012, to December 31, 2021, the monthly (intra-month) temporal coefficient of variation (CV) of water and atmospheric elements (environmental parameters) is calculated for each month and each recommended oceanic pseudo-invariant site. For each parameter, within each month and each 1°×1° grid cell, the CV was computed from the intra-month temporal mean (μ) and standard deviation (σ) derived from all observations available within that month at the dataset's native temporal resolution, and the resulting pixel-wise CV values were then spatially averaged over the grid cell to obtain a representative monthly CV for each candidate site, as shown in Eq.1.

$$\mathrm{CV} = \frac{\sigma}{\mu} \times 100\%. \tag{1}$$

The CV threshold is set to identify the grid position where the CV of each element is below the CV threshold in this month over the ten years, and the optimally selected pseudo-invariant area is obtained month by month and grid by grid. The time-series distribution information for each environmental parameter in the optimally selected grid is statistically analyzed, and the monthly 1°×1° gridded dataset of oceanic pseudo-invariant-site characteristics is finally obtained. Each record contains the month (1–12), the grid coordinates, and the decadal relative-frequency distributions for all parameters. Using this dataset, a 1°×1° grid is judged suitable when, in at least 10 of the 12 months, every parameter is at or below its CV threshold. Grids satisfying this rule define the high-suitability pseudo-invariant optimally selected grid.

2.1 Environmental parameter determination and optimal site selection method

The temporal domain variation in oceanic pseudo-invariant site radiation comprises two components: the water body and the atmospheric state within the radiometric benchmark transfer time window. Variations in TOA reflectance are driven principally by the water factor: chlorophyll-*a* (Chl-*a*) concentration; atmospheric factors: aerosol optical thickness at 550 nm (AOT_{550}), relative humidity (RH), and instantaneous 10-m wind speed (WS). Time-series of Chl *a*, AOT_{550}, RH, WS, and water-leaving reflectance (R_{rs}) at 443, 488, 555, 667, and 678 nm (see Table 2) are sourced as follows: Chl *a* and AOT_{550} are directly from MODIS data products; RH is computed from ERA5 2-m dew-point temperature (T_d) and 2-m air temperature (T) via the modified Magnus formula, whose relative error remains below 0.4% between -80 and 50 °C (Alduchov and Eskridge, 1996) as shown in Eq.2. WS is synthesized by the instantaneous vector components WS_u and WS_v of the wind speed at a

Table 2 Basic information of data products

Parameter	Dataset source (GEE collection ID)	Temporal resolution	Spatial resolution
Chl *a*, R_{rs}	NASA/OCEANDATA/MODIS-Terra/L3SMI	Daily	4 km
AOT_{550}	MODIS/061/MOD08_M3	Monthly	1°
WS_u, WS_v, T_d, T	ECMWF/ERA5/HOURLY	Hourly	0.25°

height of about 10 m from the sea surface in the two orthogonal directions of east-west (u) and north-south (v), its vector magnitude formula is given by Eq.3.

$$\mathrm{RH} = 100 \times \frac{\exp\left(\frac{17.625T_\mathrm{d}}{T_\mathrm{d}+243.04}\right)}{\exp\left(\frac{17.625T}{T+243.04}\right)}, \tag{2}$$

$$\mathrm{WS} = \sqrt{\mathrm{WS}_u^2 + \mathrm{WS}_v^2}. \tag{3}$$

In each panel of Fig.1a, the "Mean, Std, Slope, P" lists, in turn, the temporal mean, the standard deviation of the monthly series, the slope of an ordinary least-squares linear fit to all monthly data, and the associated P-value. From top to bottom, the variables are Chl a, R_{rs443}, R_{rs488}, R_{rs555}, and AOT_{550}. The two horizontal dashed lines indicate the interval, mean positive and negative 1 time the standard deviation. When most monthly values remain within this envelope, and the fitted slope is not significantly different from zero (e.g., P<0.001), the corresponding parameter can be regarded as temporally stable; persistent excursions beyond this band or a significant non-zero slope indicate a lack of stability (Li, 2022). In each panel of Fig.1b, each time series is obtained by averaging the parameter over all 1°×1° grid cells within the North Pacific gyre box (150°E–165°E, 10°N–20°N). The CV maps describe the relative spatial and temporal variability of each parameter within the region, with lower CV values indicating more homogeneous and thus more suitable optical conditions for long-term radiometric benchmark inter-satellite transfer. For

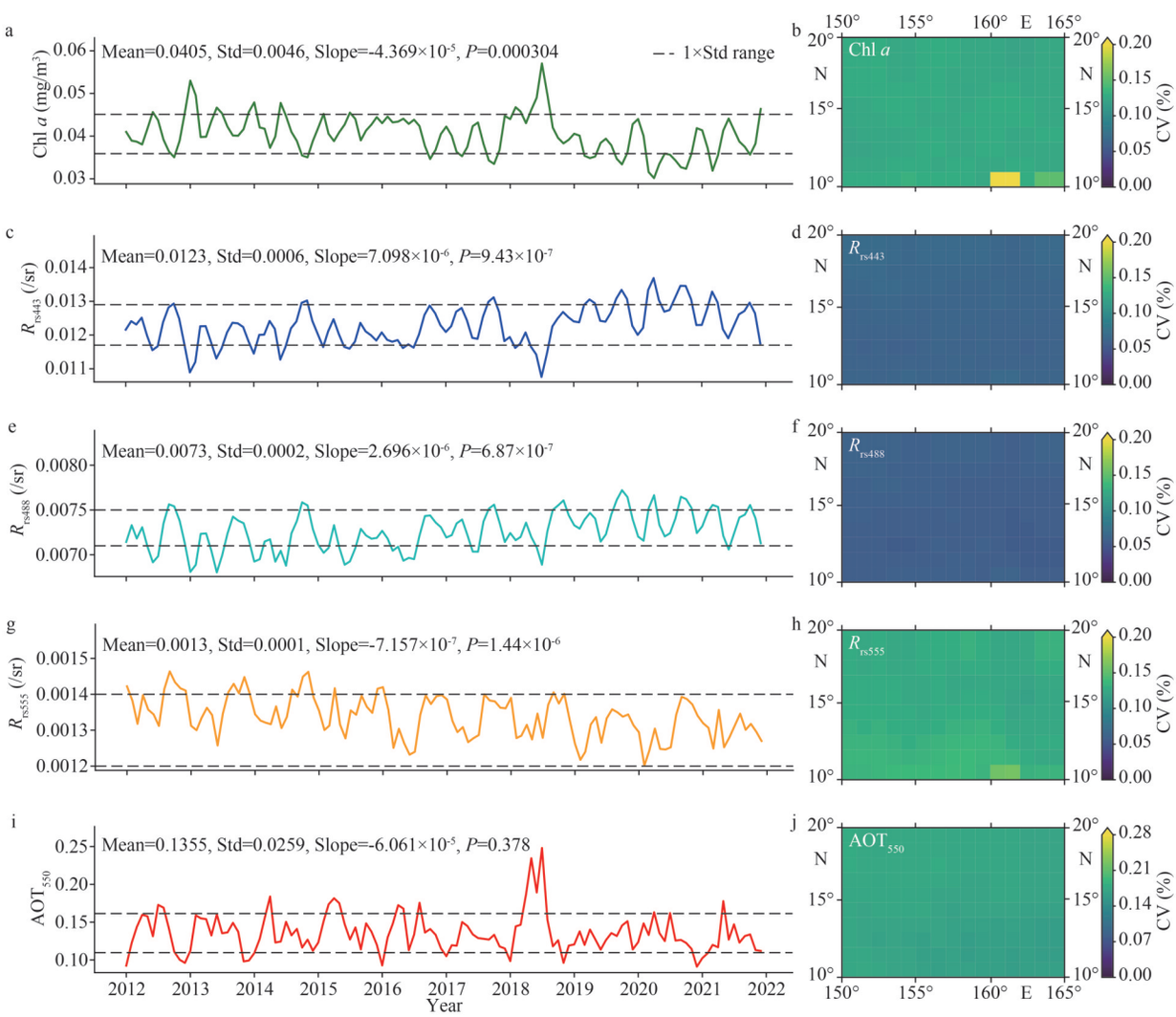

Fig.1 Monthly mean time series (left column) and 10-year mean coefficient of variation (CV; right column) of each parameter in the NPG region (150°E–165°E, 10°N–20°N) during 2012–2021

Chl *a*, AOT_{550}, and the three R_{rs} bands, the fitted slopes are tiny, and the monthly values fluctuate predominantly around one standard deviation of the mean, indicating that the water-column bio-optical properties and atmospheric aerosols at the selected site are stable over the decade.

In optimal site selection, each grid is screened based on the stability of its optical properties. In evaluating marine regions relevant to the ocean color System Vicarious Calibration (SVC), scholars such as Zibordi established optical property stability thresholds for ocean color sensors that were derived from open-ocean oligotrophic and mesotrophic waters far from continental influences. Specifically, their criteria require that the CV of remote sensing reflectance (R_{rs}), including R_{rs443}, R_{rs488}, and R_{rs555}, is less than 20%; the Chl *a* is less than 0.2 mg/m^3 and the standard deviation is less than 0.04 mg/m^3; and the standard deviation of aerosol optical thickness at 865 nm (AOT_{865}) is less than 0.03 (Zibordi and Mélin, 2017). Chen et al. (2021) adopted these core criteria to evaluate satellite vicarious calibration sites in the South China Sea and further optimized them by tightening aerosol-related constraints, which reduced the threshold for aerosol optical thickness at 869 nm (AOT_{869}) from 0.15 to 0.12, while retaining all other thresholds from previous research by Zibordi and Mélin (2017). Under these refined conditions, the optical properties of the target area can be considered stable (Chen et al., 2021). Based on the mean AOT range of 0.05–0.11 and corresponding standard deviations reported in related research by Zibordi et al. (2017), the CV of AOT is conservatively estimated as 28%. Equation 4 reflects the relationship between AOT_{550} and AOT_{869} originally formulated by Ångström (1929). Based on this relationship, the Ångström index α for clean seawater is typically low, generally ranging between 0.2 and 0.4 (Smirnov et al., 2002; Xin et al., 2026). According to the relationship in Eq.4, the smaller index is, the closer AOT_{550} and AOT_{869} become numerically. Combined with the CV calculated by Eq.1 from the average value (μ) and standard deviation (σ), it is considered that the CV values of AOT_{550} and AOT_{869} for the same clean oceanic pseudo-invariant site (the index is constant and small) should be similar. Therefore, the following thresholds were used in this study: the CV thresholds for R_{rs443}, R_{rs488}, R_{rs555}, and Chl *a* were set to 20%, and the coefficient of variation threshold of AOT_{550} was set to 28%; and the Chl *a* was required to be less than 0.2 mg/m^3.

$$\frac{AOT_{869}}{AOT_{550}} = \left(\frac{869}{550}\right)^{-\alpha}. \quad (4)$$

2.2 Optimal selection results and radiation characteristics description

According to the threshold setting in Section 2.1 above, this study divides the 1°×1° grid in the global recommended oceanic pseudo-invariant sites for screening, and finds all the grid areas that meet the threshold requirements (CV of each parameter is less than its corresponding CV threshold) in the 12 months over the ten years as the optimally selected grid. Through this process, we ensure that the selected results maintain a high degree of consistency and stability over the long term, making them suitable as the target area for radiometric benchmark transfer.

The description of the radiation characteristics of the target area primarily involves the optical and radiative properties of the ocean water body and its upper atmosphere. These parameters all affect the radiometric benchmark transfer between the reference instruments and the target instruments (ocean satellite) to varying degrees. This study intends to simulate the TOA radiation of several complex radiation contribution factors (water-interface-atmospheric layer) contained in the radiometric benchmark transfer process of the oceanic pseudo-invariant site. On this basis, a global sensitivity analysis of each selected parameter is conducted to clarify the influence mechanisms of each error source (temporal, spatial, spectral, and angular domains). Therefore, based on the grid-by-grid and month-by-month optimally selected results obtained above, combined with the dataset in Table 2, the key parameters' radiation characteristics and their extreme ranges are extracted from the filtered, effective observations (optimally selected grid) that meet the selection criteria at each grid and month, and the extreme-value statistics for each parameter at the minimum spatial and temporal resolutions are summarized in Table 3.

2.3 Suitability assessment and compilation of characteristic dataset

The monthly effective data volume (the number of months that meet the threshold requirement) for each 1°×1° spatial grid point is used as the suitability evaluation index for the inter-satellite radiometric benchmark transfer target area (grid point). The larger the monthly effective data

Table 3 Extreme-value ranges of parameters for optimally selected grid

Parameter extreme-value	Chl *a* (mg/m^3)	R_{rs443} (/sr)	R_{rs488} (/sr)	R_{rs555} (/sr)	AOT_{550}	WS (m/s)
Max.	0.212 1	0.020 9	0.011 0	0.002 5	0.382 5	25.857 4
Min.	0.007 4	0.004 1	0.003 6	0.000 5	0.049 0	0.043 2

volume, the more helpful it is to fully understand the variation law under different geographical and meteorological conditions, and the greater the suitability of applying it in radiometric benchmark transfer. In this study, a selected dynamic 1°×1° grid is considered highly suitable when the effective data volume meets the specified thresholds in at least 10 of the 12 months. In this case, grid points that satisfy this criterion can cover the four seasons in time series. The NPG grid points are shown in Fig.2; the grid points of SAG: 25.5°W–24.5°W, 18.5°S–17.5°S; and the grid points of SIG: 76.5°E–77.5°E, 22.5°S–21.5°S.

Based on the extreme value range of each parameter in Table 3, the relative-frequency distribution (first, discretize the continuous variable into intervals, and then divide the number of observations in each interval by the total number of observations to obtain a distribution that represents the relative frequency of each interval) of each parameter (AOT_{550}, RH, Chl *a*, WS) in the high-suitability pseudo-invariant optimally selected grid from January 1, 2012, to December 31, 2021 is statistically analyzed. The peak position of the fitting normal distribution is taken as the center; and the statistical group spacing width is symmetrically expanded as the step size (using the larger radius from the center on both the left and right sides). The interval closest to 90% coverage is found, as shown in Table 4.

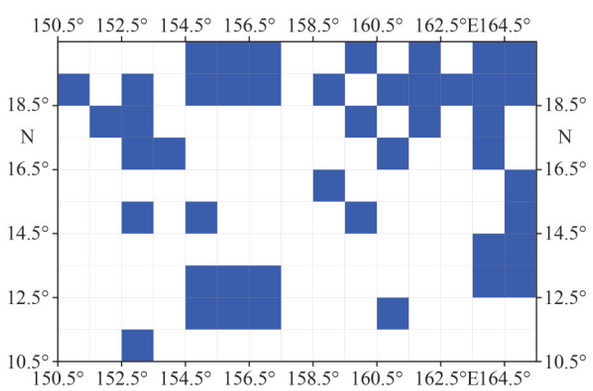

Fig.2 1°×1° grids at NPG site meeting the thresholds for ≥10 out of 12 months

Taking the statistical results of Chl *a* in Fig.3 as an example: for the five recommended oceanic pseudo-invariant sites in Fig.3a and the 47 high-suitability pseudo-invariant optimally selected grids in Fig.3b, according to the statistical group bin width in Table 4, the total histograms of 5 or 47 distributions are drawn by semi-transparent bar superposition, and the group median with the largest frequency is found as the "central peak", which is used as the symmetry axis to extend to both sides until the coverage is closest to 90% (red vertical dotted line). At the same time, according to the standard deviation of the fitting normal distribution of 5 or 47 data distributions of all data, and using the "central peak" mentioned above as the center, the normal distribution fitting curve is drawn.

Under the premise that the "central peak" is the reference value, this study focuses on the parameter differences corresponding to more than 90% of the actual state, as shown in Fig.3b. During the global sensitivity analysis of subsequent control variables, the "central peak" (e.g., Chl *a*=0.042 mg/m^3) serves as the reference value. On this basis, in the 47 high-suitability optimally selected grids, the four parameters of WS, Chl *a*, AOT_{550}, and RH are counted monthly, and the monthly-grid-by-grid data that meet the CV threshold requirements are selected. Finally, a monthly 1°×1° gridded dataset of oceanic pseudo-invariant-site characteristics is formed (contains information such as month (1–12), grid

Table 4 Information on the relative-frequency distribution of key environmental parameters

Parameter	Bin width	Approx. 90% coverage interval	Frequency
WS (m/s)	0.5	6.75±4.25	91.7
AOT_{550}	0.004	0.13±0.046	89.2
Chl *a* (mg/m^3)	0.004	0.042±0.014	87.7
RH (%)	0.5	79.25±10.25	90.0

Frequency values are given in percentage (%).

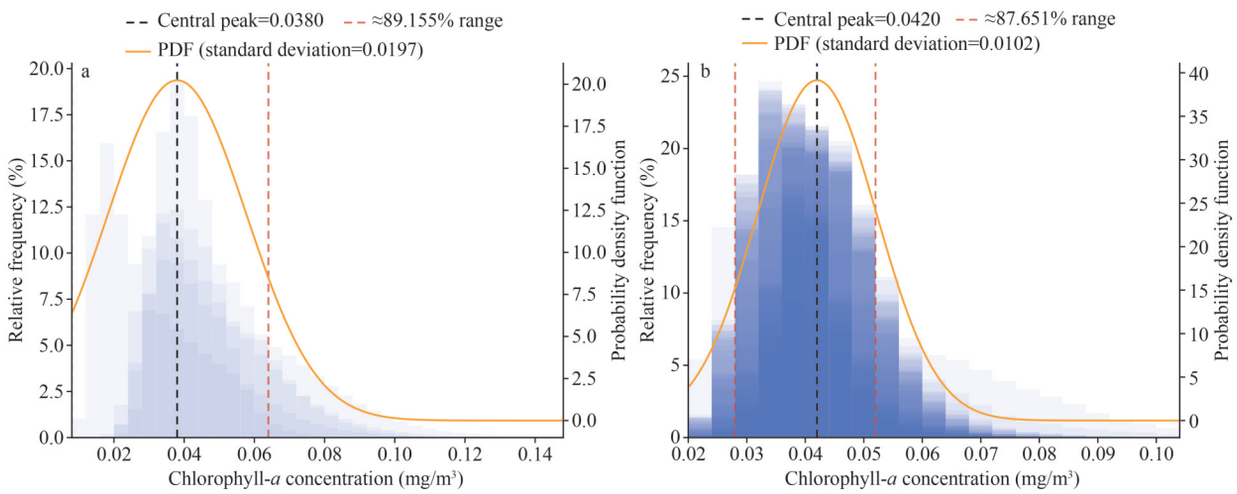

Fig.3 Total relative-frequency distributions and fitted probability density function (PDF) curves of Chl-*a* concentration for five recommended sites (a) and 47 high-suitability grids (b) during 2012–2021

coordinates, the decadal relative-frequency distribution information of all parameters: WS, AOT_{550}, Chl *a*, RH, month by month "central peak" of grid by grid, approx. 90% coverage interval, standard deviation of fitting normal distribution, etc.). This characteristic dataset serves as the statistical foundation for simulation scene construction in subsequent single-parameter sensitivity pre-screening and global sensitivity analysis. Specifically, the central-peak values derived for each parameter define the background state of the oceanic pseudo-invariant site. Parameters exhibiting weak sensitivity to top-of-atmosphere reflectance are fixed at their corresponding central-peak values. In contrast, parameters with stronger sensitivity are treated as input variables in the global sensitivity analysis. For these variables, the sampling ranges are defined by the corresponding "central-peak" values and the associated "approx. 90% coverage interval", within which low-discrepancy sequence sampling is performed.

3 METHOD

In analyzing the sources of uncertainty in the radiometric benchmark transfer process, this study qualitatively summarizes four types of error sources in the marine radiometric transfer chain: time matching, space matching, spectral matching, and observation geometry matching, based on previous research and analysis. Combined with theoretical analysis and single-parameter sensitivity pre-screening, the parameters that have a significant impact on the radiometric benchmark transfer process, based on high spatial homogeneity, temporal stability, and oligotrophic, high-suitability pseudo-invariant optimally selected grids, are summarized as input variables for global sensitivity analysis. Based on the above ideas, the OSOAA air-sea coupled RTM is used to simulate TOA reflectivity in the visible to near-infrared range, and a radiometric benchmark transfer simulation scene is constructed. Through the Sobol global sensitivity analysis and the Dual-Threshold Convergence-Based Self-Expanding Sampling (DTCSS) Method, the degree of influence and coupling effect of the transfer process of the oceanic pseudo-invariant site, which contains several complex radiation contribution factors (water-interface-atmosphere radiation), on the transfer results is clarified. The research results can be used to guide the data matching constraint process and related transfer difference uncertainty evaluation in the radiometric benchmark transfer process. The overall flow chart is shown in Fig.4.

3.1 Single-parameter sensitivity pre-screening

In this study, the radiometric benchmark transfer is carried out using oligotrophic radiometrically stable targets with high spatial and temporal homogeneity. In theory, parameters such as sediment concentration, the 440-nm debris absorption coefficient, and the 440-nm absorption coefficient of yellow matter in satellite products matching (temporal domain) are small and exhibit high spatial and temporal homogeneity. Therefore, these parameters are not used as input variables for sensitivity analysis, and the reference value is set to zero, assuming negligible contributions under

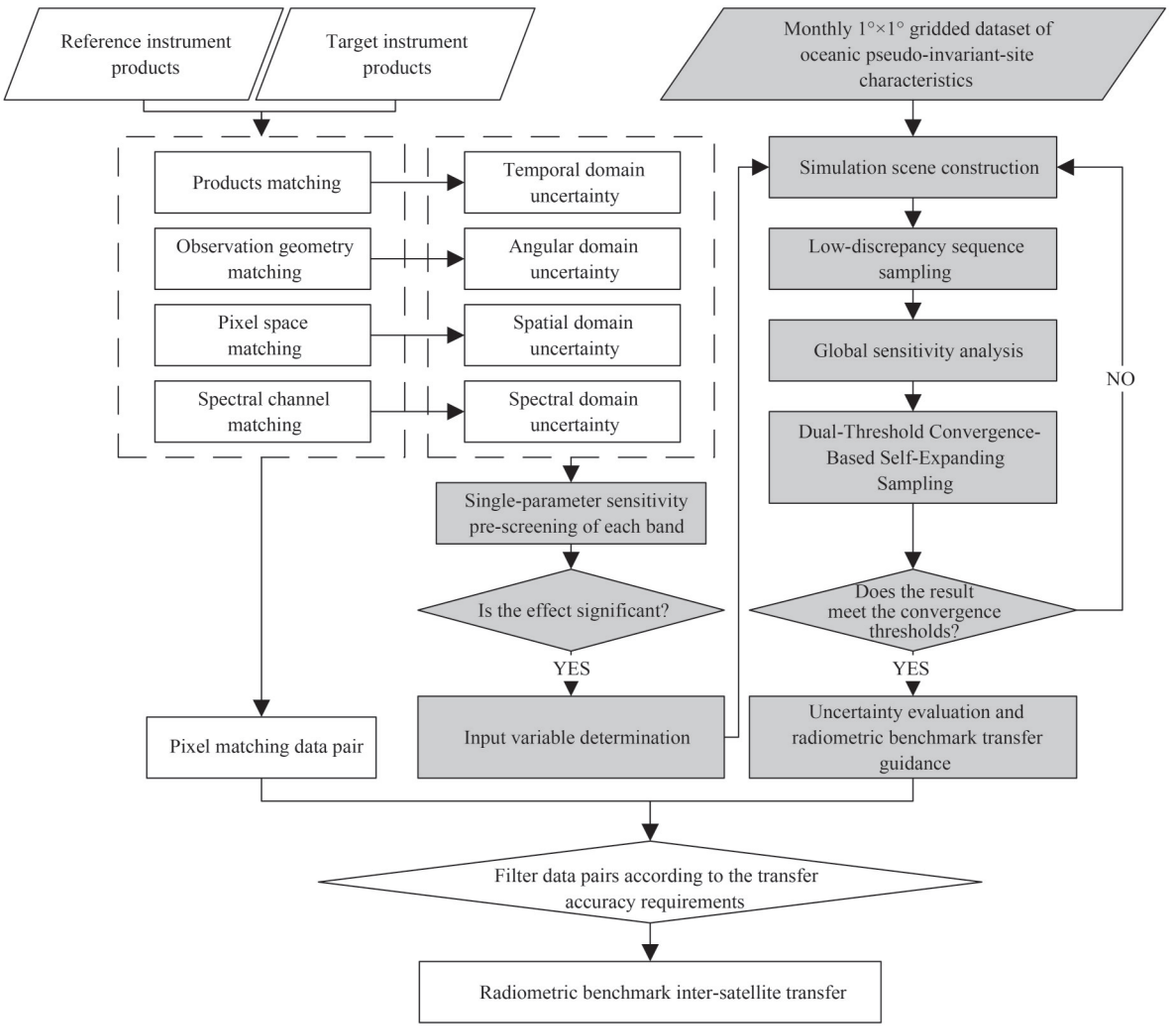

Fig.4 Global sensitivity analysis flow diagram

oligotrophic and radiometrically stable oceanic conditions. Other temporal domain parameters, such as AOT_{550}, RH, Chl *a*, etc., are evaluated using a single-parameter sensitivity pre-screening method.

In spatial matching (spatial domain), the effect of positional differences and spatial coverage differences is assumed to be negligible under the considered observation scales. The spatial domain uncertainty source is mainly reflected in differences in the sun-glint influence on the rough water-air interface across different observation scales (spatial resolutions). According to the Cox-Munk model, higher wind speeds generate larger sea-surface slopes, thereby strengthening the ocean's specular reflection (sun-glint), and excessively amplifying part of the observed radiance signal (Cox and Munk, 1954), increasing the uncertainty of radiation transmission; the existence of surface waves not only increases the geometric complexity of the sea surface but also, through wave breaking, injects bubble clouds whose scattering and absorption of incident radiation in the visible and near-infrared spectral regions modify both the spatial distribution and the magnitude of the radiance (Frouin et al., 1996; Sullivan and McWilliams, 2010). Therefore, the influence of spatial matching differences is transformed into the main parameter (i.e., wind speed) affecting sea surface roughness.

According to the observation geometric matching (angular domain) and spectral matching (spectral domain) requirements in the radiometric benchmark transfer link process from reference instruments to target instruments via oceanic pseudo-invariant sites, the angular domain parameters are summarized as: Relative Azimuth Angle (RAA), Solar Zenith Angle (SZA), Viewing Zenith Angle (VZA), and the spectral domain parameters are the central wavelength of the spectral band.

Taking the Chinese Ocean Color and Temperature Scanner (COCTS) onboard the HY-1D satellite as the target sensor (bandwidth 20 nm, center wavelength of each channel is 412, 443, 490, 520, 565, 670, 750, 865 nm, relative spectral response function RSR sequence interval 1 nm) as an example, the typical channel centered at 443 nm with a larger value is selected for analysis as an example. Based on the monthly 1°×1° gridded dataset of oceanic pseudo-invariant-site characteristics established in Section 2.3, and the relative-frequency distributions of each temporal-domain parameter in the optimally selected sites from January 1, 2012, to December 31, 2021, as shown in Fig.3. The root mean square relative error (RMS Relative Error, E_{RMS}) and the sensitivity coefficient (C) of the atmospheric top reflectivity corresponding to each parameter after the univariate offset $\pm\Delta i$ are calculated by Eqs.5 & 6, respectively. Among them, $R_{\mathrm{true},\,i}$ is the atmospheric top reflectivity without offset. After adding different offset $\pm\Delta i$, the offset atmospheric top reflectivity $R_{\mathrm{est},\,i}$ (including positive offset atmospheric top reflectivity $R_{\mathrm{est+}}$ and negative offset atmospheric top reflectivity $R_{\mathrm{est-}}$), F represents the number of samples under the offset Δi, k represents the ergodic subscript, and Δi is the equal amplitude disturbance applied by the variable in the positive and negative directions. For each parameter i, $E_{\mathrm{RMS},\,i}$ and C_i are evaluated by applying symmetric perturbations within the "Approx. 90% coverage interval" derived in Table 4, and the results are shown in Table 5.

$$E_{\mathrm{RMS},\,i}=\sqrt{\frac{1}{F}\sum_{k=1}^{F}\left[\frac{R_{\mathrm{est},\,k}-R_{\mathrm{true},\,i}}{R_{\mathrm{true},\,i}\times 2|\Delta i|}\times 100\%\right]^2}, \tag{5}$$

$$C_i=\frac{100\%\times\left[R_{\mathrm{est+}}-R_{\mathrm{est-}}\right]}{R_{\mathrm{true},\,i}\times 2|\Delta i|}. \tag{6}$$

According to the E_{RMS} and C of the atmospheric top reflectivity of each ocean series satellite band, coupled with each parameter, such as the results at 443 nm shown in Fig.5. Parameters exhibiting significant impacts on the radiometric benchmark transfer using the optimally selected oceanic pseudo-invariant site are identified and selected as input variables for the global sensitivity analysis.

3.2 Input variable determination and simulation scene construction

Based on the single-parameter sensitivity pre-screening results in Section 3.1, the parameter space of radiometric benchmark transfer is constructed, and a numerical simulation experiment is designed. The main input variables include: aerosol optical thickness at 550 nm (AOT_{550}) in the temporal domain; WS in the spatial domain; central wavelength in the spectral domain; Relative Azimuth Angle (RAA), Solar Zenith Angle (SZA), and Viewing Zenith Angle (VZA) in the angular domain. In this subsection, we first briefly introduce the coupled radiative transfer model adopted in this study and then describe the range of input variables and the construction of the simulation scene.

To simulate the transfer of radiative signals from oceanic pseudo-invariant sites to the top of the atmosphere, this study employs the OSOAA air-sea coupled vector radiative transfer model. Building on ocean-optical theory, researchers first developed scalar in-water radiative transfer models such as Hydrolight. To account for atmospheric effects and polarization, a suite of coupled atmosphere-ocean vector radiative transfer models (RTM) was later introduced, including OSOAA (Ordres Successifs Ocean Atmosphere Avance) (Chami et al., 2015), the AccuRT (Accurate Radiative Transfer) model (Hamre et al., 2017; Stamnes et al., 2018), and the PCOART (Polarized Coupled Ocean Atmosphere Radiative Transfer) model (He et al., 2010). While models like AccuRT are highly versatile, their primary function is as scalar tools assuming flat interfaces, lacking the capability to handle full polarization and rough sea-surface bidirectional effects. The advanced vector models (such as OSOAA and PCOART) typically represent the rough air-sea interface using the Cox-Munk wave-slope distribution parameterized.

OSOAA retains the advantages of earlier radiative-transfer codes while introducing atmospheric effects and polarization, yielding a more

Table 5 443-nm E_{RMS} and C result for each parameter

Result	WS	Chl *a*	AOT_{550}	RH
Source of uncertainty	Spatial domain	Temporal domain		
E_{RMS} (%)	0.360	1.064	2.631	1.349
C (%)	0.085	75.082	57.194	0.121

comprehensive and accurate representation of ocean-atmosphere radiative transfer. In particular, it has been developed to account for a rough sea surface, enabling the prediction of both radiance intensity and polarization state within the coupled system beneath a rough interface. Compared to PCOART (which relies on the matrix-operator method), OSOAA incorporates the successive orders of scattering method. This mathematical architecture makes OSOAA computationally efficient at predicting the full Stokes vector profiles at any altitude or depth, making it suited for the analysis of multi-angular and polarimetric satellite sensors. For example, its high-precision correction capability under complex atmospheric conditions has been used to model the impact of absorbing aerosols on atmospheric correction for satellite ocean color remote sensing (Song et al., 2022). Because OSOAA accounts for polarization, it has also been applied to simulate bottom-up polarization imaging of underwater targets at various depths and types (Pan et al., 2022). Owing to its flexible, multilayer treatment of atmospheric and water optical properties, OSOAA excels under demanding environmental conditions: it has been employed to simulate and analyze UV-A radiance reaching passive satellite sensors (Zhang et al., 2018); to model sea surface to the top of the atmosphere radiative signals under varying moonlight, geometry, and turbidity for nighttime detection of suspended matter (Chami et al., 2020); and to evaluate uncertainties in atmospherically corrected ocean satellite products (Tauro et al., 2022).

This study adopts the OSOAA vector radiative transfer model to simulate the coupled ocean–atmosphere system. Based on the characteristic dataset derived in Section 2, the input variables and simulation scene are defined to represent radiometrically stable oceanic pseudo-invariant sites under non-ideal matching conditions. The reference state of the simulations is defined using the central peak values of the relative frequency distributions for key environmental parameters. The variation ranges of sensitive parameters such as AOT_{550} are constrained by their corresponding approximately 90% coverage intervals derived from the characteristic dataset, while weakly sensitive parameters are fixed at their representative values for computational efficiency (e.g., RH=79.25%, Chl *a*= 0.042 mg/m^3). Considering the frequency analysis of wind speed distribution, a very small number of extreme points are deleted, and the analysis range of 0–16 m/s is taken. According to the requirements of ocean satellite radiometric benchmark transfer, the spectral parameters are set to wavelengths of particular interest for ocean, aquatic environments, wetlands, and similar applications (specifically: 40 wavelength values of 412, 431, 440, 443, 450, 473, 490, 510, 530, 550, 560, 565, 605, 620, 639, 655, 665, 670, 675, 680, 683, 695, 700, 705, 710, 715, 726, 740, 745, 750, 760, 783, 800, 815, 830, 842, 865, 890, 940, 945 nm), to cover typical ocean remote sensing visible and near-infrared bands; the observation geometric matching conditions are set according to the possible differences between the reference instruments and the target instruments. The RAA considers the two extreme cases of 0° and 180° to cover the strongest and weakest polarization sun-glint. At the same time, when the SZA exceeds 70°, the performance of the Chl-*a* extraction algorithm in satellite data verification is significantly reduced, leading to a substantial increase in error (Li et al., 2017a). Using the above settings, a radiometric transfer simulation scene covering various possible matching-difference conditions is established, as shown in Table 6.

3.3 Low-discrepancy sequence sampling and global sensitivity analysis

The multi-dimensional parameter space determined in the previous Section 3.2 uses a low-discrepancy sequence sampling method. In this study, the spectral dimension is treated discretely, and global sensitivity analysis is performed independently at each of the selected 40 wavelength values rather than including wavelength as a continuous input variable in the Sobol analysis. The low-discrepancy sequence enables uniform and efficient sampling within each parameter range, providing faster

Table 6 Reference values of input parameters for OSOAA simulations

Domain	Input parameter	Variation range
Temporal	AOT_{550}	0.13±0.046
Spatial	WS (m/s)	0–16
Spectral	Wavelength (nm)	40 discrete values
Angular	SZA (°)	0–70
Angular	VZA (°)	0–90
Angular	RAA (°)	0–180
–	Aerosol type	Marine aerosols
–	Submarine depth (m)	500
–	Seafloor albedo	0

convergence and enhanced variance reduction. The sample size N is chosen as a power of 2 to ensure numerical convergence and computational efficiency in the estimation of sensitivity indices. For each group of input variable value combinations, the OSOAA model is called to forward simulate the atmospheric top reflectivity as the result of the simulated observation under the corresponding conditions of the reference instrument or the target instrument. A large number of simulated sample outputs are stored as the data basis for global sensitivity analysis. On this foundation, a variance-based global sensitivity analysis is carried out to quantify how uncertainties in the input parameters propagate to the TOA reflectance.

For this purpose, this study applies Sobol-based Global Sensitivity Analysis (Sobol-GSA) (Sobol, 1990): a technique that couples a variance decomposition framework with Monte Carlo numerical integration and partitions the output variance exactly into each input factor's first-order contribution and the higher-order interaction terms (Sobol, 2001; Saltelli et al., 2010). In addition, this study employs a quasi-Monte Carlo scheme driven by low-discrepancy sequences uniformly and incrementally populates the k-dimensional unit hypercube, greatly increasing coverage of the parameter space and filling the gaps left by purely random draws; such sequences routinely outperform crude Monte Carlo and Latin-hypercube sampling and exhibit faster convergence than the rate of ordinary Monte Carlo, achieving comparable or superior estimation accuracy with far fewer samples, advantages that make them suitable for global sensitivity analysis of complex models (Ökten and Liu, 2021). By comparison, other GSA techniques, such as the Morris screening method, deliver only a qualitative ranking of factors and disregard higher-order interactions, making them appropriate for preliminary screening but inadequate for supporting a global uncertainty evaluation (Saltelli et al., 2010). Moreover, Sobol-GSA imposes no monotonicity assumption and is valid for any square-integrable "black-box" model (Homma and Saltelli, 1996). Consequently, this study adopts Sobol-GSA driven by low-discrepancy sequence sampling as a superior option for quantifying inter-parameter effects while balancing analytical accuracy and computational efficiency.

In practice, the Sobol-GSA is used here to quantitatively describe the influence of independent and coupling changes in each parameter in the multi-dimensional parameter space of this study on atmospheric top reflectivity output through variance decomposition. Specifically, the Sobol-GSA is performed on the "input variable value combination" and "atmospheric top reflectivity output" dataset obtained by the simulation. The process of defining the radiometric benchmark transfer link is a "black box", that is, each discrete wavelength defines a group of five input variables X_1, X_2, $\cdots$, X_5 (i.e., VZA, SZA, RAA, AOT_{550}, WS) determined in Section 3.1, then the model Y=function (X_1, X_2, $\cdots$, X_5) of is decomposed into the form of Eq.7 by the variance decomposition Var (Y) .

$$\mathrm{Var}(Y)=\sum_{i=1}^{5}V_i+\sum_{i<j}V_{ij}+\cdots+V_{1,2,\cdots,5}, \tag{7}$$

where V_i is the contribution of the i input variables, V_{ij} is the contribution of the interaction between the i and j input variables, and $V_{1,2,\cdots,5}$ is the output variance generated by the simultaneous interaction of all five variables. Based on this decomposition, the first order index S_i shown in Eq.8, the total effect sensitivity index ST_i, of Eq.9, and the second order index S_{ij} of Eq.10 are obtained. Firstly, the variance decomposition principle is used to calculate the proportion of output variance caused by a single variable i when other variables are fixed randomly, which is used to describe the contribution rate of a single input variable to the output atmospheric top reflectivity deviation when it changes alone, that is, the first order index S_i of Eq.8. At the same time, the total effect sensitivity index ST_i of Eq.9 is calculated to evaluate the full impact of a single variable i, including the interaction on the output, that is, the part $V_{\sim i}$ which excludes parameter i is subtracted from the whole. Moreover, the second order index S_{ij} of Eq.10 between two parameters i and j is calculated to identify the significant coupling effect between two parameters.

$$S_i=\frac{V_i}{\mathrm{Var}(Y)}, \tag{8}$$

$$\mathrm{ST}_i=1-\frac{V_{\sim i}}{\mathrm{Var}(Y)}, \tag{9}$$

$$S_{ij}=\frac{V_{ij}}{\mathrm{Var}(Y)}. \tag{10}$$

According to the variance-decomposition relation Eq.7, all orders of Sobol sensitivity indices are theoretically non-negative (Sobol, 2001). In practice, however, when the index's actual value is

zero or extremely close to zero, the estimator may return a negative number with a very small absolute value. Hence, this study adopts a threshold approach: any index with an estimated value of 10^{-5} or less is deemed to make no appreciable contribution to the output, and only positive sensitivity indices are subsequently analyzed.

3.4 Dual-Threshold Convergence-Based Self-Expanding Sampling (DTCSS)

Increasing the number of random samples can theoretically improve analysis accuracy, but once a certain number is reached, it becomes impossible to distinguish whether the difference in results is due to random number selection or to the increase in the number of random samples. To take into account the accuracy and computational efficiency of the result calculation, according to the experimental method in the above Section 3.3, this study performed five independent repeated experiments without interference (m=1, ⋯ , 5) between each five input variables i (i.e., VZA, SZA, RAA, AOT_{550}, WS). For each input variable i: First, within each run m=M (i.e., the Mth experiment), the first order index $S_{i_{N_M}}$ and total effect sensitivity index $ST_{i_{N_M}}$ were estimated at each successive sample size N=2^x (x≤15, N_{max}=32 768, the experimental results show that: 2^{2-14} is usually sufficient), the average values (i.e., $\bar{S}_{i_{N_M}}$ and $\overline{ST}_{i_{N_M}}$) are calculated, and then the standard deviation (i.e., $\sigma_{S_{i,N}}$ and $\sigma_{ST_{i,N}}$) obtained by Eqs. 11 & 12. Second, across all five experiments, the changes between adjacent samplings ($\Delta S_{i,N}$ and $\Delta ST_{i,N}$) obtained by Eqs.13 & 14, i.e., in the n_1 (n_1 is the fixed value N−1) sampling of all 5 experiments, the $S_{i_{(N-1)_M}}$ and $ST_{i_{(N-1)_M}}$ of the results were calculated, and in the n_2 (n_2 is the fixed value N), can similarly obtain $S_{i_{N_M}}$ and $ST_{i_{N_M}}$, and then, the absolute value between the calculated results of $S_{i_{(N-1)_M}}$ and $S_{i_{N_M}}$, $ST_{i_{(N-1)_M}}$ and $ST_{i_{N_M}}$ are $\Delta S_{i,N}$ and $\Delta ST_{i,N}$, and the mean value of $\Delta S_{i,N}$ and $\Delta ST_{i,N}$ obtained by Eqs.15 & 16 is the threshold of the changes between adjacent samplings. When the standard deviation $\sigma_{S_{i,N}}$, $\sigma_{ST_{i,N}}$ and the $\Delta S_{i,N}$, $\Delta ST_{i,N}$ are less than the threshold value respectively, the judgment result is considered convergent and record the best N value at this time, otherwise N is increased until the criteria are met.

$$\sigma_{S_{i,N}} = \sqrt{\frac{1}{N-1}\sum_{n=1}^{N}\left(S_{i_{N_M}} - \bar{S}_{i_{N_M}}\right)^2}, \tag{11}$$

$$\sigma_{ST_{i,N}} = \sqrt{\frac{1}{N-1}\sum_{n=1}^{N}\left(ST_{i_{N_M}} - \overline{ST}_{i_{N_M}}\right)^2}, \tag{12}$$

$$\Delta S_{i,N} = \left| S_{i_{N_M}} - S_{i_{(N-1)_M}} \right|, \tag{13}$$

$$\Delta ST_{i,N} = \left| ST_{i_{N_M}} - ST_{i_{(N-1)_M}} \right|. \tag{14}$$

The specific threshold requirement is that the single simulation (m=M) standard deviation $\sigma_{S_{i,N}}$ and $\sigma_{ST_{i,N}}$ is less than 0.05; and the changes between adjacent samplings $\Delta S_{i,N}$ is less than $\overline{\Delta S}_{i,n,mean}$ ($\Delta ST_{i,N}$ is less than $\overline{\Delta ST}_{i,n,mean}$).

$$\overline{\Delta S}_{i,n,mean} = \frac{1}{M}\sum_{m=1}^{M}\left| S_{i_{n_m}} - S_{i_{(n-1)_m}} \right|, \tag{15}$$

$$\overline{\Delta ST}_{i,n,mean} = \frac{1}{M}\sum_{m=1}^{M}\left| ST_{i_{n_m}} - ST_{i_{(n-1)_m}} \right|. \tag{16}$$

4 RESULT AND DISCUSSION

4.1 Convergence trend of the sensitivity index with sample size

The DTCSS method described in Section 3.4 is applied to expand the sampling size N automatically and to analyze the convergence behavior of the sensitivity indices with increasing N, thereby determining an optimal sample size that balances computational efficiency and accuracy. The S_i or ST_i of the five repeated experiments at 443 nm, shown in Fig.5, was plotted with the sample size N between 2^7 and 2^{15}, and the error bar was drawn with the standard deviation of the same N in the five repeated experiments. Specifically, in the process of calculating S_i or ST_i for each variable i, the optimal sampling number N is different, but more than 95% of the cases across all variables and replicate runs indicate that the optimal sampling size lies between 2^{12} to 2^{14} for this band. The results show that when N reaches approximately 2^{14} the standard deviation of the five variables is less than 0.05, and the changes between adjacent samplings are less than the threshold among all five variables in almost all cases, indicating that further increasing the number of samples only amplifies the random noise without increasing the amount of information.

4.2 Global sensitivity analysis result

The global sensitivity analysis was carried out at 40 discrete wavelength points spanning 412 to 945 nm, covering the typical spectral bands from the visible to the near-infrared commonly used in

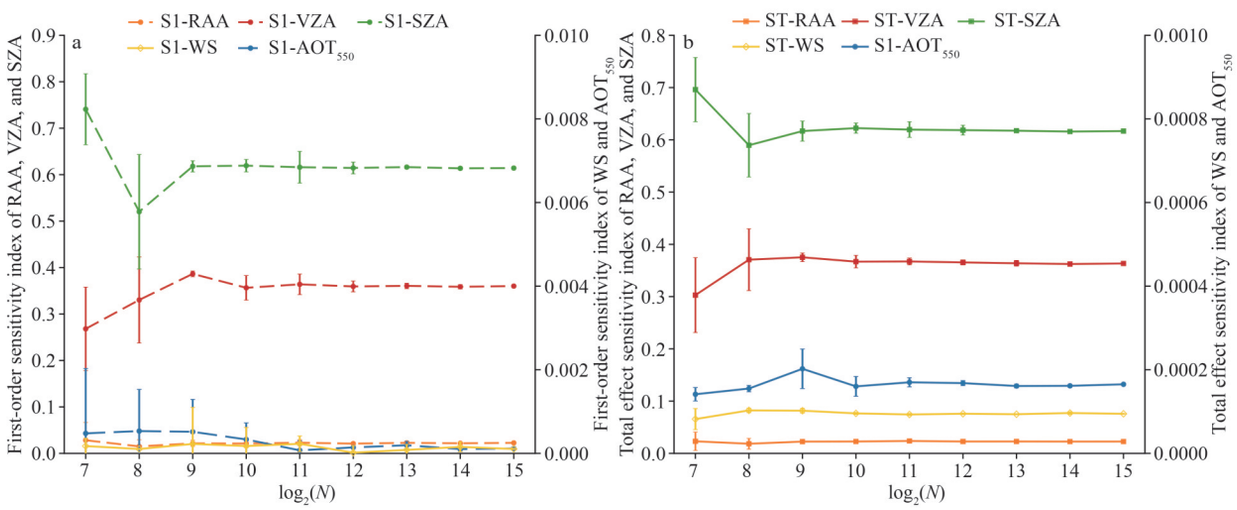

Fig.5 Trend of the sensitivity index with sample size for five replicate experiments at 443 nm: S_i (a) and ST_i (b) for the five input factors (AOT_{550}, RAA, WS, SZA, and VZA)

marine remote sensing. Combined with the method of Sections 3.3 & 3.4 and the best sample size N confirmed in Section 4.1 above, and the first order index S_i of the five independent experiments are averaged, the results are shown in Fig.6. The observation geometry in the angular domain dominates the S_i of the atmospheric top reflectivity. Concretely speaking, the SZA is the primary influencing factor in the short-wave blue band and its S_i can reach more than 0.6 and decreases monotonically with the wavelength; the sensitivity associated with RAA increases in an approximately complementary manner to that of SZA, intersects with SZA near 655–665 nm and quickly becomes the primary factor, and the total effect accounts for more than 0.6 after 760 nm; the monotonicity of the VZA is similar to that of SZA, but the contribution reaches a peak of about 0.35–0.4 in the 443–565 nm range, and then decreases rapidly to nearly 0.1. In contrast, the sensitivity of AOT_{550}, and wind speed is always lower than 0.02, which can be considered negligible in comparison with the angular-domain parameters, indicating that these two types of time-domain and spatial-domain error sources contribute less to the reflectivity than the angular domain under radiometrically stable sea surface conditions. In summary, this study concludes that the overall sensitivity influence degree is stable as "angular domain (RAA, SZA)>angular domain (VZA)≫ temporal domain (AOT_{550}) and spatial domain (wind speed)".

The underlying physical mechanisms driving this spectral transition can be explained by considering the dominant radiative processes at different wavelengths. At shorter wavelengths (Blue-Green Bands), Rayleigh scattering dominates the TOA signal with its characteristic λ^{-4} dependence (Penndorf, 1957). The magnitude of this path radiance is primarily controlled by the atmospheric optical path length, which geometrically depends on sec(SZA)+sec(VZA), especially the total radiance at TOA increases with VZA due to the increase in atmospheric path length (He et al., 2014). In contrast, at longer wavelengths (red to NIR), the physical mechanism reverses. Due to strong absorption by water molecules, the water-leaving radiance becomes negligible (Mishra et al., 2014). Consequently, the TOA signal is predominantly governed by aerosol scattering and sea-surface sun-glint. Both the aerosol scattering phase functions and the rough sea-surface specular reflection (characterized by the Cox-Munk distribution) exhibit extreme directional anisotropy that is heavily dependent on the RAA (Gordon and Wang, 1994). A peak in the BRDF arises from sunglint when the Sun and satellite viewing angles are similar and oriented in a forward scattering geometry (Fasnacht et al., 2019). This strong anisotropy, together with the negligible water-leaving radiance in the red-NIR bands, makes RAA the dominant source of variance at longer wavelengths. Moreover, as explicitly demonstrated in Fig.6, the S_i of all geometric and atmospheric drivers display exceptionally smooth, monotonic, and continuous gradients across the 400–950-nm continuum. There are no abrupt non-linear jumps between adjacent discrete bands. This strict

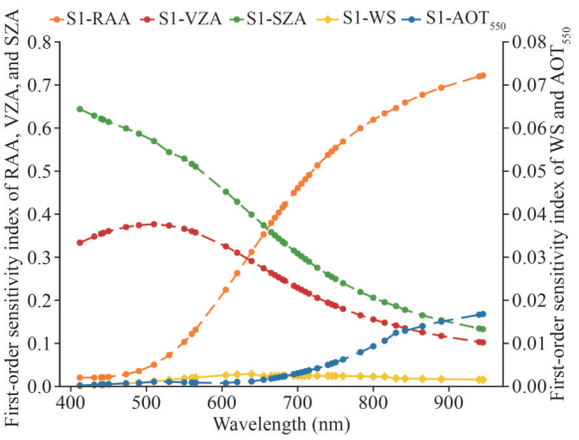

Fig.6 Global sensitivity analysis at 40 discrete wavelengths between 412 and 945 nm

spectral continuity mathematically guarantees the robustness and physical reliability of high-precision sensitivity interpolation (e.g., using cubic splines) between anchor bands. Instead of the computationally prohibitive task of simulating thousands of narrow bands in GSA, finer-resolution hyperspectral validation will focus primarily on the critical 660-nm crossover wavelength between SZA and RAA, where 1 nm or PACE's native interval narrowband sampling is sufficient to quantify subtle shifts in the dominance transition boundary without the need for complex full-spectrum localized reconstruction.

Further analysis of the ST_i shows that its curve almost coincides with S_i, indicating that the additional contribution of high-order interactions to the output variance is very weak, and the first-order effect has essentially captured the results of the model variance decomposition. According to the variance decomposition theory in Section 3.3, if the total effect sensitivity index ST_i is equal to the first order index S_i, the model is completely additive (there is no interaction), and the S_i of each input variable satisfies the additive sum of 1; when the model contains interactions, the interaction variance occupies a part of the output variance alone, so that the sum of S_i is less than 1. Taking the results of global sensitivity analysis at 443 nm as an example, Table 7 shows that the sum of the S_i is very close to unity. This indicates that the variance of the interaction is weak at this wavelength. The above viewpoint is verified by the results of the second order index S_{ij} shown in Fig.7.

Table 7 Result of S_i and ST_i at 443 nm

Parameter	RAA	VZA	SZA	WS	AOT_{550}
S_i	0.021 74	0.360 59	0.614 45	0.000 15	0.000 19
ST_i	0.022 76	0.367 24	0.618 53	0.000 01	0.000 16

Based on S_i and the S_{ij} results from five repeated experiments, all parameters were scaled to optimal magnitudes via the DTCSS automatic sampling expansion method. The S_i is placed on the main diagonal, and S_{ij} is filled into the upper triangles of a matrix to build the heat map (the lower triangles of this matrix are omitted only for visual clarity, because it is numerically identical to the upper triangle and would therefore be redundant). The map is drawn to obtain the parameter interaction distribution relationship shown in Fig.7. From this figure, we can see the interaction between the parameters more intuitively: the AOT_{550} has little effect on the output results and the influence of wind speed on the output results is also small, both have a coupling relationship with the VZA and RAA, but the coupling S_{ij} value is less than 0.005 and can therefore be considered insignificant; the sensitivity of the SZA and the VZA under the independent action is relatively high. There is a coupling relationship among the three variables related to the observation geometry, but the values remain significantly lower than S_i, indicating that although the observation geometric parameters at 443 nm have an interactive effect on the influence of the top-of-atmosphere reflectance, this effect is mainly reflected in the single-parameter drive. In summary, temporal, spatial, spectral, and angular uncertainty domains are relatively independent at 443 nm. The descending order of parameter impacts on TOA reflectance at 443 nm is: SZA>VZA>RAA>AOT_{550}≈WS.

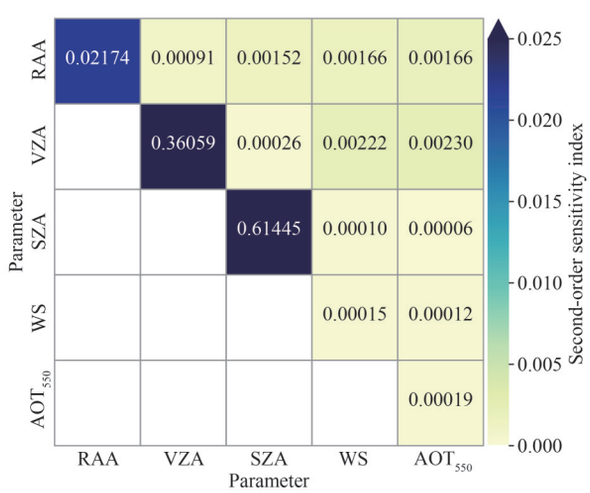

Fig.7 The second-order sensitivity S_{ij} index at 443 nm

4.3 Uncertainty evaluation and radiometric benchmark transfer guidance

According to the results in Fig.6, among the five key parameters that have a significant impact on the radiometric benchmark transfer of marine radiometrically stable targets, the influence and interactions on the results vary by band. Thus, inter-satellite matching constraint design and transfer uncertainty quantification should be implemented on a band-by-band basis according to the results in Sections 3.3 & 3.4.

When guiding radiometric benchmark inter-satellite data matching constraints, the dominant source of uncertainty in the marine satellite radiometric benchmark transfer process can be analyzed and assessed using calculated sensitivity indexes. Focus on the factors with a higher first order index and total effect sensitivity index, and use the results of the global sensitivity analysis to guide benchmark transfer. On the one hand, the main sources of uncertainty are identified, and their contribution to the influence of atmospheric top radiation is quantified. On the other hand, we can loosen strict matching rules or simplify processing for minor factors in practical inter-satellite benchmark transfer. If necessary, the radiometric benchmark transfer method can be improved based on the results of global sensitivity analysis. For example, we can build empirical correction models for top-contributing factors to lower their induced uncertainty. In addition, global sensitivity analysis can also verify the rationality of the selection of oceanic radiometrically stable targets. If the analysis shows that some environmental parameters, which have less influence on the optimally selected pseudo-invariant target sites, still exhibit large uncertainty. In that case, it is necessary to re-screen for more stable areas or further constrain the observation-matching conditions in radiometric benchmark transfer.

Specifically, the first order index is used to rank the influence of each input variable on the output. The more sensitive the influence is, the stricter the constraint conditions required for the variable in the radiometric benchmark transfer process are. Thus, angular parameter matching between reference and target sensors follows the strictest rules in benchmark transfer. According to the relative numerical size of the total effect sensitivity index and the first order index, the strength of the coupling effect between the variable and other variables is judged. If inter-parameter coupling effects on TOA reflectance are negligible (over two orders of magnitude lower than individual parameter effects), such interactions can be disregarded. In this case, the reflectance uncertainty introduced by differences in multiple input variables can be approximated by a functional relationship between the total effect sensitivity indices and the difference of the single input variation. From the global sensitivity analysis in Section 4.2, the combined standard uncertainty of four uncertainty sources is the sum of standard uncertainties of individual parameters in each domain.

For each uncertainty domain, parameter variation thresholds δ_i between reference and target satellites match the "Approx. 90% coverage interval" in Table 4 (e.g., wind speed threshold is 4.25 m/s). Figure 3 analysis shows all parameters follow approximate Gaussian temporal distributions with fixed peak values and standard deviation σ_i. Per GUM's uncertainty propagation rules, we calculate coverage factor k from the matching Gaussian function. If the parameter distribution remains unknown, adopt uniform distribution and set $k=\sqrt{3}$. We then compute each parameter's standard uncertainty u_i (k=1) by dividing RMS by k (JCGM, 2008). These individual uncertainties are then summed to yield the combined uncertainty standard U (k=1) from a single uncertainty source. To place the "approximately 90% coverage" RMS effects on a metrologically rigorous footing, Eqs.17 & 18 are reformulated as:

$$k_i = \frac{\delta_i}{\sigma_i}, \tag{17}$$

$$U = \sqrt{\sum_{i=1}^{g} u_i^2} = \sqrt{\sum_{i=1}^{g} \left(\frac{E_{\mathrm{RMS},i}}{k_i} \right)^2}. \tag{18}$$

In Eqs.17 & 18, i=1, ⋯, g stands for input parameters including VZA, SZA, RAA, AOT_{550}, and WS. $E_{\mathrm{RMS},i}$ denotes TOA reflectance RMS error caused solely by $\pm\delta_i$ offset on the ith parameter. σ_i refers to standard deviation of fitted normal distribution. k_i is the variable's coverage factor; its ideal value for 90% Gaussian coverage is 1.645, while practical values derive from measured distributions.

According to the Single-parameter sensitivity pre-screening result in Section 3.1, the uncertainty calculation results provide a list of parameters that need to be corrected or constrained in the data-matching method for each band, along with the

corresponding upper limit for the uncertainty. To translate these theoretical uncertainty bounds into practical implementable guidance for inter-satellite data matching, this study hereby recommends a hierarchical matching framework constrained by the above uncertainty limits. First, temporal-spatial climatology matching is adopted: low-temporal-variability monthly spatial grids are prioritized, and climatological background parameters (e.g., WS, AOT_{550}, Chl *a*, and RH) are set to their long-term "central peaks" in the monthly 1°×1° gridded dataset of oceanic pseudo-invariant-site to quantify controllable temporal uncertainty, enabling flexible intra-month observation pairing without strict simultaneous overpass requirements. We calculate radiometric uncertainty from using climatological "central peak" values instead of instantaneous data via Eqs.5, 17, and 18. On this basis, geometric tolerance gating is implemented in accordance with the parameter sensitivity hierarchy: for ocean-color critical blue-green bands, solar and viewing zenith angle differences between reference and target sensors are strictly confined within 1° to suppress dominant angular-induced uncertainty. Finally, stringent pixel-level spatial homogeneity matching is performed, with 0.05° maximum nearest-neighbor distance and 5×5 moving window coefficient of variation threshold below 3% to eliminate dynamic oceanic and aerosol microscale perturbations.

5 CONCLUSION AND FUTURE WORK

Based on the simulation results of the OSOAA radiative transfer model, a multi-band atmospheric top reflectance sample library covering the 412–945-nm range was constructed, explicitly accounting for sea-air coupling effects and employing Sobol global sensitivity analysis with low-discrepancy sequence sampling. Meanwhile, the "Dual-Threshold Convergence-Based Self-Expanding Sampling (DTCSS)" framework was developed and applied. Across five independent global sensitivity analysis experiments without mutual interference, the best sample size N was quantitatively between 2^{12} and 2^{14} (results differ across different bands and parameters), which effectively avoids the noise amplification caused by oversampling while balancing computational efficiency and analytical accuracy. In addition, the global sensitivity analysis of 40 discrete wavelengths reveals that the angular domain geometry (SZA, RAA, VZA) is the dominant factor influencing the change in atmospheric top reflectivity. Specifically, SZA exhibits the highest contribution in the shortwave blue band, and RAA rapidly becomes dominant in the red to near-infrared band. The first-order contribution of the two parameters accounts for the vast majority of the total effects, indicating that the higher-order interactions contribute negligibly to output variance. The influence of AOT_{550} in the temporal domain and wind speed in the space domain on the reflectivity consistently remains below 0.02, and can therefore be considered negligible under radiometrically stable sea-surface conditions. The overall sensitivity hierarchy remains stable across wavelengths, following the order "RAA and SZA $\gg$ VZA $\gg$ AOT_{550} and WS". At 443 nm, the second-order Sobol interaction indices are further confirmed to be negligible, indicating that first-order effects alone account for nearly all of the variance. These findings reinforce that the observation geometry (SZA, RAA, VZA) is the dominant source of uncertainty in top-of-atmosphere reflectance, which is consistent with the conclusions of multiple LUT-based sensitivity studies employing 6S and BRDF models, which identified viewing and solar geometry as the primary drivers of TOA variability (Amini et al., 2021). Moreover, these results are consistent with PICS-based TOA radiometric reference modeling, which leverages the temporal characteristics of stable land targets, representing the geometry as main variability and modeling seasonal atmospheric effects within constrained angular ranges, meeting an acceptable relative-difference result without ground data (Ma et al., 2025), further supporting the interpretation that angular factors play a leading role in the stable-site transfer framework. Together, these results provide a solid theoretical basis for subsequent uncertainty quantification and model simplification in radiometric benchmark transfer over oceanic optimally selected pseudo-invariant sites.

The current discrete-band sensitivity analysis results satisfy the radiometric benchmark transfer matching requirements of China's HY-1 series ocean satellites, while additional improvements are needed for sensors with narrower spectral intervals. For hyperspectral payloads, including the upcoming Radiometric Benchmark Satellite and Ocean Color Instrument (OCI) onboard the PACE satellite, the results across 412–945 nm need to be extended to continuous spectra. This work suggests a differentiated technical solution to balance computational load and simulation accuracy. Cubic

spline interpolation is used to derive continuous spectral results from discrete GSA outputs for general spectral bands. For the critical crossover near 660 nm where the dominant contribution switches between SZA and RAA, we recommend finer sampling. The sampling interval is flexibly configured according to the actual spectral specifications of hyperspectral instruments for radiometric benchmark transfer. In future research, this sampling and interpolation scheme will be validated using in-orbit PACE-OCI L1B data. Reflectance from blue and red bands will be grouped by observation geometry (SZA, RAA, VZA) to conduct real-scenario verification. For a single radiometric benchmark inter-satellite transfer link, the uncertainty for an individual pixel pair can be estimated using the framework presented in Section 4.3. However, two-scene matching typically produces multiple pixel-level data pairs. For results obtained under comparable spatiotemporal and angular conditions, the data-fusion and uncertainty-evaluation framework for multi-frequency inter-satellite radiometric benchmark transfer can be employed to integrate multiple pixel-level results in a statistically robust manner (Dai et al., 2025). According to China's Radiometric Benchmark Satellite scheme, geometric co-observation modes include the orbit-crossover mode, the geostationary co-observation mode, the synchronous lunar observation mode, and the Lagrange-point mode; these enable high-accuracy star-to-star radiometric value transfer through co-sourced observations, providing a unified radiometric reference for operational satellites (Lu et al., 2020). With the benchmark satellite(s) and other reference missions in orbit, multiple operational satellites are expected to share a unified radiometric scale through co-observation and spectral convolution with the target sensor's spectral response functions, thereby enabling high-accuracy inter-satellite radiometric benchmark transfer. This harmonized radiometric reference is expected to substantially reduce cross-platform mosaicking errors and uncertainties in long-term global Level-3 and Level-4 products, providing a solid foundation for integrated ocean-land-atmosphere climate monitoring and data assimilation.

6 DATA AVAILABILITY STATEMENT

All data generated and analyzed during this study are available from the corresponding author on reasonable request.

References

Alduchov O A, Eskridge R E. 1996. Improved Magnus form approximation of saturation vapor pressure. *Journal of Applied Meteorology*, **35**(4): 601-609, https://doi.org/10.1175/1520-0450(1996)035<0601:IMFAOS>2.0.CO;2.

Amini S, Momeni M, Monadjemi A. 2021. Sensitivity analysis of look-up table for satellite-based aerosol optical depth retrieval. *Journal of Aerosol Science*, **158**: 105842, https://doi.org/10.1016/j.jaerosci.2021.105842.

Angal A, Xiong X X, Wu A S et al. 2016. On-orbit performance and calibration improvements for the reflective solar bands of Terra and Aqua MODIS. *In*: Proceedings Volume 9881, Earth Observing Missions and Sensors: Development, Implementation, and Characterization IV. SPIE, New Delhi, India. https://doi.org/10.1117/12.2223912.

Ångström A. 1929. On the atmospheric transmission of sun radiation and on dust in the air. *Geografiska Annaler*, **11**(2): 156-166, https://doi.org/10.1080/20014422.1929.11880498.

Chami M, Lafrance B, Fougnie B et al. 2015. OSOAA: a vector radiative transfer model of coupled atmosphere-ocean system for a rough sea surface application to the estimates of the directional variations of the water-leaving reflectance to better process multi-angular satellite sensors data over the ocean. *Optics Express*, **23**(21): 27829-27852, https://doi.org/10.1364/OE.23.027829.

Chami M, Larnicol M, Migeon S et al. 2020. Potential for nocturnal satellite detection of suspended matter concentrations in coastal waters using a panchromatic band: a feasibility study based on VIIRS (NASA/NOAA) spectral and radiometric specifications. *Optics Express*, **28**(10): 15314-15330, https://doi.org/10.1364/OE.393048.

Chen J, He X Q, Liu Z L et al. 2020. An approach to cross-calibrating multi-mission satellite data for the open ocean. *Remote Sensing of Environment*, **246**: 111895, https://doi.org/10.1016/j.rse.2020.111895.

Chen J, Xu N, He X Q et al. 2022. Determining pseudo-invariant calibration sites for comparing inter-mission ocean color data. *ISPRS Journal of Photogrammetry and Remote Sensing*, **192**: 377-394, https://doi.org/10.1016/j.isprsjprs.2022.08.004.

Chen S G, Song Q J, Ma C F et al. 2021. Evaluation of regions suitable for vicarious calibration of ocean color satellite sensors in the South China Sea. *Optics Express*, **29**(8): 11712-11727, https://doi.org/10.1364/OE.423108.

Cox C, Munk W. 1954. Measurement of the roughness of the sea surface from photographs of the sun's glitter. *Journal of the Optical Society of America*, **44**(11): 838-850, https://doi.org/10.1364/JOSA.44.000838.

Dai C H, Wang Y F, Wu Z F et al. 2025. Data fusion and uncertainty evaluation method for inter-satellite radiation dissemination. *Acta Optica Sinica*, **45**(24): 2428006, https://doi.org/10.3788/AOS250999. (in Chinese with English abstract)

Dournaux M, Tulet P, Pianezze J et al. 2025. Origin, size distribution, and hygroscopic properties of marine

aerosols in the southwestern Indian Ocean: results of six campaigns of shipborne observations. *Atmospheric Chemistry and Physics*, **25**(17): 10315-10335, https://doi.org/10.5194/acp-25-10315-2025.

Fasnacht Z, Vasilkov A, Haffner D et al. 2019. A geometry-dependent surface Lambertian-equivalent reflectivity product for UV-Vis retrievals—Part 2: evaluation over open ocean. *Atmospheric Measurement Techniques*, **12**(12): 6749-6769, https://doi.org/10.5194/amt-12-6749-2019.

Fougnie B, Henry P, Morel A et al. 2002. Identification and characterization of stable homogeneous oceanic zones: climatology and impact on in-flight calibration of space sensors over Rayleigh scattering. *In*: Proceedings of Ocean Optics XVI. Santa Fe, NM, USA. p.18-22.

Fox N, Green P. 2020. Traceable radiometry underpinning terrestrial- and helio-studies (TRUTHS): an element of a space-based climate and calibration observatory. *Remote Sensing*, **12**(15): 2400, https://doi.org/10.3390/rs12152400.

Frouin R, Schwindling M, Deschamps P Y. 1996. Spectral reflectance of sea foam in the visible and near-infrared: in situ measurements and remote sensing implications. *Journal of Geophysical Research*: *Oceans*, **101**(C6): 14361-14371, https://doi.org/10.1029/96JC00629.

Gatebe C K, King M D, Lyapustin A I et al. 2005. Airborne spectral measurements of ocean directional reflectance. *Journal of the Atmospheric Sciences*, **62**(4): 1072-1092, https://doi.org/10.1175/JAS3386.1.

Goldin D, Xiong X X, Shea Y et al. 2019. CLARREO Pathfinder/VIIRS intercalibration: quantifying the polarization effects on reflectance and the intercalibration uncertainty. *Remote Sensing*, **11**(16): 1914, https://doi.org/10.3390/rs11161914.

Gordon H R. 1997. Atmospheric correction of ocean color imagery in the Earth Observing System era. *Journal of Geophysical Research*: *Atmospheres*, **102**(D14): 17081-17106, https://doi.org/10.1029/96JD02443.

Gordon H R, Wang M H. 1994. Retrieval of water-leaving radiance and aerosol optical thickness over the oceans with SeaWiFS: a preliminary algorithm. *Applied Optics*, **33**(3): 443-452, https://doi.org/10.1364/AO.33.000443.

Gorroño J, Banks A C, Fox N P et al. 2017. Radiometric inter-sensor cross-calibration uncertainty using a traceable high accuracy reference hyperspectral imager. *ISPRS Journal of Photogrammetry and Remote Sensing*, **130**: 393-417, http://dx.doi.org/10.1016/j.isprsjprs.2017.07.002.

Gorroño J, Solé M P, Fox N, et al. 2024. Global assessment of directional effects in the intercalibration of optical satellite instruments with the TRUTHS mission. *IEEE Transactions on Geoscience and Remote Sensing*, **62**: 5536313, https://doi.org/10.1109/TGRS.2024.3483969.

Hamre B, Stamnes S, Stamnes K et al. 2017. AccuRT: a versatile tool for radiative transfer simulations in the coupled atmosphere-ocean system. *AIP Conference Proceedings*, **1810**: 120002, https://doi.org/10.1063/1.4975576.

Hannadige N K, Zhai P W, Gao M et al. 2023. Performance evaluation of three bio-optical models in aerosol and ocean color joint retrievals. *Atmospheric Measurement Techniques*, **16**(23): 5749-5770, https://doi.org/10.5194/amt-16-5749-2023.

He X Q, Pan D L, Bai Y et al. 2010. Rough sea-surface model for vector radiative transfer of coupled ocean-atmosphere system. *Acta Optica Sinica*, **30**(3): 618-624, https://doi.org/10.3788/AOS20103003.0618. (in Chinese with English abstract)

He X Q, Pan D L, Bai Y et al. 2014. A new simple concept for ocean colour remote sensing using parallel polarisation radiance. *Scientific Reports*, **4**(1): 3748, https://doi.org/10.1038/srep03748.

Holmes A, Morrison J M, Feldman G et al. 2018. Hawkeye ocean color instrument: performance summary. *In*: Proceedings Volume 10769, CubeSats and NanoSats for Remote Sensing II. SPIE, San Diego, California, United States. p.87-101, https://doi.org/10.1117/12.2320654.

Homma T, Saltelli A. 1996. Importance measures in global sensitivity analysis of nonlinear models. *Reliability Engineering & System Safety*, **52**(1): 1-17, https://doi.org/10.1016/0951-8320(96)00002-6.

Hu Q, He Y Q, Xu N et al. 2024. Cross calibration over sites and uncertainty assessment for reflective solar bands. *National Remote Sensing Bulletin*, **28**(8): 2045-2061, https://doi.org/10.11834/jrs.20232095. (in Chinese with English abstract)

Joint Committee for Guides in Metrology(JCGM). 2008. Evaluation of measurement data—Guide to the expression of uncertainty in measurement (GUM). JCGM 100: 2008, https://doi.org/10.59161/JCGM100-2008E.

Li H, HeX Q, BaiYet al. 2017a. Assessment of satellite-based chlorophyll-*a* retrieval algorithms for high solar zenith angle conditions. *Journal of Applied Remote Sensing*, **11**(1): 012004, https://doi.org/10.1117/1.JRS.11.012004.

Li W K. 2022. Spatio-temporal Stability Analysis of Calibration Site and Temporal Degradation Correction of Instrument Response for Ocean Color Remote Sensing. Wuhan University, Wuhan, China, https://doi.org/10.27379/d.cnki.gwhdu.2022.003141. (in Chinese with English abstract).

Li Z Q, Guo J P, Ding A J et al. 2017b. Aerosol and boundary-layer interactions and impact on air quality. *National Science Review*, **4**(6): 810-833, https://doi.org/10.1093/nsr/nwx117.

Lu N M, Ding L, Zheng X B et al. 2020. Introduction of the radiometric benchmark satellite being developed in China for remote sensing. *Journal of Remote Sensing*, **24**(6): 672-680, https://doi.org/10.11834/jrs.20200011. (in Chinese with English abstract)

Ma L L, Zhao Y G, Li W et al. 2025. Top-of-atmosphere radiometric reference model for stable land sites with relaxed temporal stability requirements and its application to GF6/WFI radiometric calibration and validation. *Remote Sensing of Environment*, **326**: 114796, https://doi.org/10.1016/j.rse.2025.114796.

Mishra N, Helder D, Angal A et al. 2014. Absolute calibration of optical satellite sensors using Libya 4 Pseudo invariant calibration site. *Remote Sensing*, **6**(2): 1327-1346, https://doi.org/10.3390/rs6021327.

Morel A, Claustre H, Gentili B. 2010. The most oligotrophic

subtropical zones of the global ocean: similarities and differences in terms of chlorophyll and yellow substance. *Biogeosciences*, **7**(10): 3139-3151, https://doi.org/10.5194/bg-7-3139-2010.

Ökten G, Liu Y N. 2021. Randomized quasi-Monte Carlo methods in global sensitivity analysis. *Reliability Engineering & System Safety*, **210**: 107520, https://doi.org/10.1016/j.ress.2021.107520.

Pan T F, He X Q, Zhang X et al. 2022. Experimental study on bottom-up detection of underwater targets based on polarization imaging. *Sensors*, **22**(8): 2827, https://doi.org/10.3390/s22082827.

Penndorf R. 1957. Tables of the refractive index for standard air and the rayleigh scattering coefficient for the spectral region between 0.2 and 20.0 μ and their application to atmospheric optics. *Journal of the Optical Society of America*, **47**(2): 176-182, https://doi.org/10.1364/JOSA.47.000176.

Qiao H Y, Lee Z, Wang D S et al. 2025. One-step retrieval of water-quality parameters from satellite top-of-atmosphere measurements. *Remote Sensing of Environment*, **323**: 114709, https://doi.org/10.1016/j.rse.2025.114709.

Sakerin S M, Golobokova L P, Kabanov D M et al. 2022. Spatial distribution of aerosol characteristics over the South Atlantic and Southern Ocean using multiyear (2004-2021) measurements from Russian Antarctic expeditions. *Atmosphere*, **13**(3): 427, https://doi.org/10.3390/atmos13030427.

Saliba G, Chen C L, Lewis S et al. 2020. Seasonal differences and variability of concentrations, chemical composition, and cloud condensation nuclei of marine aerosol over the North Atlantic. *Journal of Geophysical Research*: *Atmospheres*, **125**(19): e2020JD033145, https://doi.org/10.1029/2020JD033145.

Saltelli A, Annoni P, Azzini I et al. 2010. Variance based sensitivity analysis of model output. Design and estimator for the total sensitivity index. *Computer Physics Communications*, **181**(2): 259-270, https://doi.org/10.1016/j.cpc.2009.09.018.

Smirnov A, Holben B N, Kaufman Y J et al. 2002. Optical properties of atmospheric aerosol in maritime environments. *Journal of the Atmospheric Sciences*, **59**(3): 501-523, https://doi.org/10.1175/1520-0469(2002)059<0501:OPOAAI>2.0.CO;2.

Sobol' I M. 1990. On sensitivity estimation for nonlinear mathematical models. *Matematicheskoe Modelirovanie*, **2**(1): 112-118, https://www.mathnet.ru/eng/mm2320. (in Russian)

Sobol' I M. 2001. Global sensitivity indices for nonlinear mathematical models and their Monte Carlo estimates. *Mathematics and Computers in Simulation*, **55**(1-3): 271-280, https://doi.org/10.1016/S0378-4754(00)00270-6.

Song Z G, He X Q, Bai Y et al. 2022. Effect of the vertical distribution of absorbing aerosols on the atmospheric correction for satellite ocean color remote sensing. *IEEE Transactions on Geoscience and Remote Sensing*, **60**: 4206212, https://doi.org/10.1109/TGRS.2022.3151219.

Song Z G, He X Q, Bai Y et al. 2023. Atmospheric correction of absorbing aerosols for satellite ocean color remote sensing over coastal waters. *Remote Sensing of Environment*, **290**: 113552, https://doi.org/10.1016/j.rse.2023.113552.

Stamnes K, Hamre B, Stamnes S et al. 2018. Progress in forward-inverse modeling based on radiative transfer tools for coupled atmosphere-snow/ice-ocean systems: a review and description of the AccuRT model. *Applied Sciences*, **8**(12): 2682, https://doi.org/10.3390/app8122682.

Stramska M, Petelski T. 2003. Observations of oceanic whitecaps in the north polar waters of the Atlantic. *Journal of Geophysical Research*: *Oceans*, **108**(C3): 3086, https://doi.org/10.1029/2002JC001321.

Sullivan P P, McWilliams J C. 2010. Dynamics of winds and currents coupled to surface waves. *Annual Review of Fluid Mechanics*, **42**(1): 19-42, https://doi.org/10.1146/annurev-fluid-121108-145541.

Sun L, Hu X Q, Guo M H et al. 2012. Multisite calibration tracking for FY-3A MERSI solar bands. *IEEE Transactions on Geoscience and Remote Sensing*, **50**(12): 4929-4942, https://doi.org/10.1109/TGRS.2012.2215613.

Tauro C B, Floreani R E, Godoy F E et al. 2022. Advances in the algorithms for the generation of science products of the SABIA-Mar mission. *In*: 2022 IEEE Biennial Congress of Argentina (ARGENCON). IEEE, San Juan, Argentina. p.1-7, https://doi.org/10.1109/ARGENCON55245.2022.9940002.

Teillet P M, Barsi J A, Chander G et al. 2007. Prime candidate Earth targets for the post-launch radiometric calibration of space-based optical imaging instruments. *In*: Proceedings Volume 6677, Earth Observing Systems XII. SPIE, San Diego, California, United States, https://doi.org/10.1117/12.733156.

Xin J Y, Ma Y N, Zhang X G et al. 2026. Investigation of natural and anthropogenic effects on aerosols optical properties over the Western Pacific ocean by the research vessel KEXUE. *Journal of Environmental Sciences*, **159**: 596-605, https://doi.org/10.1016/j.jes.2025.04.001.

Zhang Y, Mao Z, Tao B et al. 2018. Simulation and analysis of UV-A radiance reaching the passive satellite sensors over case-I and case-II waters. *In*: Proceedings Volume 10784, Remote Sensing of the Ocean, Sea Ice, Coastal Waters, and Large Water Regions 2018. SPIE, Berlin, Germany, https://doi.org/10.1117/12.2325528.

Zibordi G, Johnson B C, Kwiatkowska E et al. 2025. System vicarious calibration for climate and global long-term operational ocean color applications. *Bulletin of the American Meteorological Society*, **106**(2): E394-E407, https://doi.org/10.1175/BAMS-D-24-0085.1.

Zibordi G, Mélin F. 2017. An evaluation of marine regions relevant for ocean color system vicarious calibration. *Remote Sensing of Environment*, **190**: 122-136, https://doi.org/10.1016/j.rse.2016.11.020.